

Universal low-temperature Ohmic contacts for quantum transport in transition metal dichalcogenides

Shuigang Xu^{1†}, Zefei Wu^{1†}, Huanhuan Lu^{1†}, Yu Han¹, Gen Long¹, Xiaolong Chen¹, Tianyi Han¹, Weiguang Ye¹, , Yingying Wu¹, Jiangxiazhi Lin¹, Junying Shen¹, Yuan Cai¹, Yuheng He¹, Fan Zhang², Rolf Lortz¹, Chun Cheng³, Ning Wang^{1}*

¹Department of Physics and Center for 1D/2D Quantum Materials, the Hong Kong University of Science and Technology, Clear Water Bay, Hong Kong, China

²Department of Physics, the University of Texas at Dallas, Richardson, Texas 75080, USA

³Department of Materials Science and Engineering and Shenzhen Key Laboratory of Nanoimprint Technology, South University of Science and Technology, Shenzhen 518055, China

[†]These authors contributed equally

**Corresponding author: phwang@ust.hk*

Abstract

Low carrier mobility and high electrical contact resistance are two major obstacles prohibiting explorations of quantum transport in TMDCs. Here, we demonstrate an effective method to establish low-temperature Ohmic contacts in boron nitride encapsulated TMDC devices based on selective etching and conventional electron-beam evaporation of metal electrodes. This method works for most extensively studied TMDCs in recent years, including MoS₂, MoSe₂, WSe₂, WS₂, and 2H-MoTe₂. Low electrical contact resistance is achieved at 2 K. All of the few-layer TMDC devices studied show excellent performance with remarkably

improved field-effect mobilities ranging from $2300 \text{ cm}^2/\text{V s}$ to $16000 \text{ cm}^2/\text{V s}$, as verified by the high carrier mobilities extracted from Hall effect measurements. Moreover, both high-mobility n-type and p-type TMDC channels can be realized by simply using appropriate contact metals. Prominent Shubnikov–de Haas oscillations have been observed and investigated in these high-quality TMDC devices.

Keywords: Transition metal dichalcogenides, h-BN encapsulation, field-effect-transistor, Quantum oscillations

Introduction

Experimental studies on the electrical transport properties of atomically thin semiconducting transition metal dichalcogenides (TMDCs) [1-9] have encountered a number of obstacles, such as high impurity, low carrier mobility, and high electrical contact resistance caused by Schottky barriers formed at the metal-TMDC interfaces [10, 11]. Ohmic contacts between metals and TMDCs are difficult to achieve because of work function mismatches and Fermi level pinning effects [12]. Over the last few years, significant efforts have attempted to improve the quality of electrical contacts in metal-TMDCs, such as through using work function-matched metals [13], vacuum annealing [14], and phase engineering [15]. The quality of electrical contacts at metal-WSe₂ interfaces, for example, have been gradually improved by surface doping treatment [11] and utilization of different materials with low (or tunable) work functions [10, 16]. Electrical contact problems (mainly due to Schottky barriers) exist in all semiconducting TMDC devices contacted using metal electrodes particularly at cryogenic temperatures. They significantly limit the injection of charge carriers into the transport channel and thus prohibit detection of quantum transport properties in these 2D materials. Reducing the Schottky barrier at metal-TMDC interfaces is the most critical step in advancing the device transport performance of TMDCs. Recently, ultrahigh electron mobility has been achieved in MoS₂ devices constructed based on graphene multi-terminal electrodes [17]. The contact resistance in these graphene-terminated devices can be largely reduced by applying a large back gate voltages, and quantum oscillations have been detected which show complicated multi-band features.

Based on our systematic investigations of electrical contacts in various TMDCs, we find

that cleanliness of TMDC interfaces is the critical issues in realizing high-quality Ohmic contacts and fabricating high performance devices. To eliminate the contamination/oxidation occurring on TMDC surfaces, we use a dry transfer technique in an inert environment of argon or nitrogen and protect few-layer TMDCs using ultrathin hexagonal boron nitride (h-BN) sheets [18]. Ultrathin h-BN is well-known dielectric material that provides a charge-free environment for high-quality graphene devices [19, 20]. Ultrathin h-BN is also very effective in blocking charge impurities from the SiO₂ substrate and hence increasing carrier mobility in TMDCs, particularly at low temperatures. To achieve high-quality Ohmic contacts, we develop a selective etching process to open windows from the top h-BN cover layer and deposit metal electrodes using standard electron-beam (e-beam) lithography and conventional e-beam evaporation techniques. This method is different from the edge contact configuration [20] of h-BN encapsulated graphene. The electrical Ohmic contacts prepared on the top surfaces of TMDCs by this simple etching process are very stable and can survive in air for several months (see figure S12 in Supporting Information). High field-effect mobilities of up to 16000 cm²/V s (Hall mobilities of up to 9900 cm²/V s) have been routinely achieved in n-type TMDCs. Furthermore, high mobility p-type TMDCs channels are achieved using Pd contacts since Pd has a high work function and can match the valence bands of TMDCs. As an example, high quality p-type WSe₂ with hole mobility of up to 8550 cm²/V s is demonstrated. The fabrication of high quality metal electrodes for atomically thin TMDCs demonstrated here is more practical and reliable since the contact resistance weakly depends on applied gate voltages. Remarkable improvements in contact resistance and carrier mobility allow us to observe prominent quantum phenomena, such as Shubnikov–de Haas (SdH) oscillations, in good agreement with

the intrinsic properties of the band structures in few-layer TMDCs.

Results and discussion

1. Fabrication of metal contacts for h-BN encapsulated TMDCs

Figure 1 schematically illustrates the fabrication of a field-effect transistor (FET) device from a few-layer TMDC encapsulated by h-BN sheets. The high-quality single crystalline TMDCs used in this work are either obtained commercially (e.g., MoS₂) or grown via the chemical vapor transport method (e.g., WSe₂, WS₂, MoSe₂, and 2H-MoTe₂) [21]. Few-layer TMDC samples are mechanically exfoliated on a Si substrate coated with 300 nm-thick SiO₂. To eliminate possible contamination, a polymer-free dry transfer technique recently developed for device fabrication of graphene is adopted in this study [20]. A few-layer TMDC is picked up from the SiO₂/Si substrate by an ultrathin h-BN flake through van der Waals interactions. The h-BN/TMDC flake is then transferred to a fresh h-BN flake previously exfoliated on another SiO₂/Si substrate to form a h-BN/TMDC/h-BN sandwich structure. A high temperature annealing process (under H₂/Ar atmosphere) is necessary to remove the small bubbles formed at the interfaces between h-BN and TMDCs. Although edge contacts can be established for our samples, the contact resistance is normally high, resulting in difficulties in detecting the intrinsic properties of TMDCs (see Supporting Information). The poor performance of the devices with edge contacts indicates that even TMDCs are encapsulated by h-BN sheets, if the contact problems are not solved, the intrinsic properties of the TMDC devices cannot be detected. By contrast, the etching process we developed (etching the top of h-BN only) can largely reduce the TMDC contact resistance. The contact areas are patterned by standard e-beam lithography techniques, and the exposed top h-BN layer is subsequently etched by O₂

plasma at a relatively high speed. By controlling the etching duration, TMDCs can be partially exposed for metal deposition because the etching rate of TMDCs by O₂ plasma is low.

2. Low-temperature Ohmic contacts for TMDC channel materials

To demonstrate the Ohmic contact characteristics of our TMDC devices, I_{ds}-V_{ds} measurements are first carried out in a two-terminal configuration at both room and cryogenic temperatures. Figures 2(a)-(c) display typical examples of the I_{ds}-V_{ds} curves measured under different back gates (V_g) for few-layer n-type WSe₂, p-type WSe₂, and n-type MoSe₂, respectively. Excellent Ohmic contact characteristics are maintained at 2 K. In our TMDC samples, the linear characteristics of the I_{ds}-V_{ds} curves are held from 2 K to 300 K (see figure S3 in Supporting Information). Moreover, the linearity and zero Schottky barrier height extracted from the Arrhenius plot (see figure S5 in Supporting Information) can be held at different back gate voltages (figures 2(a)-(c)). Different from graphene-TMDCs contacts [22-24], the metal contact resistance fabricated by the present etching process is weakly dependent of gate voltages.

By comparing the electrical contact characteristics of two- and four-terminal configurations, the contact resistance is extracted according to [25, 26] $R_c = R_{2p} - \frac{L_{tot}}{L_{in}} R_{4p}$, where L_{tot} and L_{in} are the total and inner channel lengths, respectively. For n-type WSe₂, the contact resistance is only 50 Ω at V_g=35 V and saturates to 150 Ω at high gate voltages (see figure S9 in Supporting Information). Given that the width of the channel is 7.0 μm and that both source and drain contributions are considered, the unit length contact resistance is within the range of 0.2–0.5 kΩ · μm, which is considerably lower than those achieved in ionic liquid gating graphene/WSe₂ (2 kΩ · μm) [10] and in Ag/WSe₂ (6.5 kΩ · μm) [16] contacts. The

most efficient contact resistances achieved by MoSe₂ and MoS₂ are about 0.3 k Ω · μ m ($V_g=70$ V) and 0.5 k Ω · μ m ($V_g=80$ V), respectively. The low contact resistance in our samples is as efficient as those achieved in metal/MoS₂ contacts by nickel-etched graphene electrodes (0.2 k Ω · μ m) [27] and by phase engineering (0.2–0.3 k Ω · μ m) [15]. The low contact resistances reported by these work [15, 27] were achieved at room temperature. In the present study, the low contact resistances we achieved have been extended to cryogenic temperatures.

We believe that the excellent performance of the metal contacts we developed should not be due to doping effects although the surfaces of few-layer TMDC channels are etched more or less by the oxygen plasma. We have used Raman spectroscopy to characterize possible impurities which might be induced by the etching process (see figure S20 in Supporting Information). However, no doping related Raman shift can be detected [28]. This is consistent with the fact that the high mobility p-type WSe₂ devices with high-quality low temperature Ohmic contacts can be easily fabricated using Pd as the contact electrodes. If our oxygen plasma etched TMDC windows areas (for making the electrodes) are heavily n-type doped, it is not possible to realize the hole injection through the Pd electrodes since the Fermi level should be pinned at the conduction band. The control experiments shown in figures S6 and S7 in Supporting Information demonstrate that the quality of the contacts and thus the performance of the TMDC devices fabricated by the etching process are highly dependent on both bottom and top h-BN sheets. Obviously, the h-BN sheets play an important role in achieving Ohmic contacts in our TMDC samples.

We find that the contact barrier for electron injection is very low if Ti (low work function) is used as the contact metal. In this case, the barrier for the hole injection is very high and no

hole injection is observed even under a large negative gate voltage. In contrast, if Pd (high work function) is used as the electrodes, the contact barrier is very low for hole (p-type) injection but very high for electron injection. In this case, we cannot observe any electron injection under a large positive gate voltage. For the devices fabricated on SiO₂/Si substrates, because the charge traps and disorder formed at the TMDCs/SiO₂ interface induce a large number of interfacial gap states and result in a high Schottky barrier with the Fermi level pinned to the band gap of the TMDCs at the contact region. Therefore, the barriers for both electron and hole injections are large but smaller than the bandgap. Therefore, the devices showed ambipolar behaviors when either Ti or Pd is used as the contact metals (see figures S13 and S14 in Supporting Information).

3. Mobility characterization for TMDC devices

Figure 3 shows the temperature-dependent transport characteristics of several TMDCs. The Ti contacted WSe₂ device shows n-type behaviors as revealed by the increasing conductance with increasing positive gate voltages, while the Pd contacted WSe₂ shows p-type behaviors. Under high gate voltages, the conductance (measured by the four-terminal configuration) dramatically increases at low temperatures. As demonstrated in a n-type WSe₂ sample, at V_g=70 V, the resistance dramatically decreases from 13720 Ω (at room temperature) to 290 Ω at 1.7 K.

Our few-layer TMDC devices exhibit excellent performance at low temperatures because of their barrier-free contacts. The field-effect mobility is extracted from the linear region of the conductance curves [4] using $\mu = [dG/dV_g] \times [\frac{L}{WC_g}]$, where L and W are the channel length and width, respectively, and C_g is the gate capacitance (the thickness of SiO₂ is 300 nm). In

this study, C_g is extracted from the Hall effect measurements, which is considered a more accurate method [29, 30]. At 2K, the field-effect mobilities achieved in n-type WS_2 , MoS_2 , WSe_2 , $MoSe_2$ and $MoTe_2$ are 16000, 14000, 8600, 4400 and 2300 $cm^2/V s$, respectively, which are summarized in table 1.

The etching process reported here is also very effective for making high quality Ohmic contact to semiconducting 2H phase $MoTe_2$ channels which have been reported to be unstable in air [31]. The 2H- $MoTe_2$ FET devices fabricated using our method show excellent performance with high mobility up to 2300 $cm^2/V s$ at 2 K. The reproducibility of this kind of high-quality samples is acceptable (more than 15 high quality devices have been obtained). Table S1 in Supporting Information summarizes the performances of our TMDC devices. The present selective etching method is applicable to ultrathin TMDCs with thickness down to two layers indicating that the etching process can be controlled fairly well. Although the mobilities of these extremely thin samples show quality degradation, the mobilities we achieved in bilayer and trilayer (1200 $cm^2/V s$ and 3900 $cm^2/V s$ respectively), for example, are considerably high. We believe that minor defect states are introduced by the O_2 plasma and degrade the quality of ultrathin thin TMDC contact channels. However, compared with the impurities induced gap states from SiO_2 , the damage or defects induced by O_2 plasma are insignificant. According to our investigation, the h-BN encapsulation structure can effectively reduce the charge traps in TMDC devices. The h-BN/TMDC/h-BN sandwich structures do not exhibit any hysteresis effect (see figure S2 in Supporting Information). However, pronounced hysteresis effects are observed in the WSe_2 devices directly prepared on SiO_2/Si substrates (see details in Supporting Information).

The temperature-dependent field-effect mobility and Hall mobility data of few-layer TMDC devices are plotted in log scale in figures 3(d)–3(g). At high temperature regions (e.g. above ~ 40 K for n-type WSe₂), the mobility is suppressed by phonon scattering, which can be fitted by $\mu \sim T^{-\gamma}$. The saturation of μ suggests impurity-dominated scattering at low temperatures. The Hall mobility is extracted according to $\mu_H = \sigma/ne$, where $\sigma = GL/W$ is the sheet conductance, $n = 1/R_H e$ is the carrier density, R_H is the Hall coefficient, and e is the charge of an electron. For n-type WSe₂, the room temperature μ_F is 105 cm²/V s and reaches 8600 cm²/V s at T=2 K. The μ_H can reach 7100 cm²/V s for a carrier density of 5.1×10^{12} cm⁻² at T=2 K. The temperature-dependent μ_H shows a characteristic similar to that of μ_F (figure 3(b)), with $\gamma = 1.9$ extracted from both μ_F and μ_H . Similarly high mobilities are also observed in MoS₂ and MoSe₂. The phonon-related parameters γ in all of the TMDCs are generally larger than those reported previously [14, 30, 32]. We observe that μ_H varies with the carrier densities. This is because when the carrier density is high, free electrons can screen the charge impurities [33] resulting in increasing μ_H with increasing carrier density ($d\mu_H/dn > 0$), as shown in the Supporting Information. The dependence of Hall mobility on carrier density also results in a larger field-effect mobility compared with the Hall mobility in the same sample (i.e., the Hall factor $r_H > 1$) [14] because $\mu_{\text{Field}} = \mu_H + nd\mu_H/dn$.

4. Shubnikov-de Haas oscillations in TMDCs

Because of the reliable low-temperature Ohmic contacts and high mobilities, the SdH oscillations of the magnetoresistance (MR) can be easily detected in our TMDC devices. Figures 4(a) and 4(e) show the R_{xx} plotted as a function of magnetic fields at different gate voltages for few-layer p-type and n-type WSe₂, respectively. Pronounced oscillations are

clearly visible in the MR data. These quantum oscillations arise from Landau quantization of the cyclotron motion of charge carriers [34]. They depend only on the perpendicular component of the applied magnetic field as verified by the field-angle dependence experiment shown in Supporting Information, revealing the 2D nature of charge carriers in few-layer WSe₂.

The temperature dependence of SdH oscillations in p-type few-layer WSe₂ at low magnetic fields is plotted in figure 4(b), in which a polynomial background is subtracted in order to extract the oscillation amplitude. At low magnetic fields in which the Zeeman effect is negligible, the SdH amplitude can be well described by the Lifshitz–Kosevich formula [35] $\Delta R(B, T) = R_D \lambda(B, T) / \sinh \lambda(B, T)$. $R_D = \exp(-2\pi^2 m^* k_B T_D / \hbar e B)$ is the Dingle factor, and $\lambda(B, T) = 2\pi^2 m^* k_B T / \hbar e B$ is the parameterized thermal damping, where k_B is the Boltzman constant, \hbar is the reduced Planck constant, and m^* is the cyclotron effective mass. Figure 4(c) shows the fitting results of the SdH oscillations in a p-type WSe₂ sample, which yield $m^* = 0.44m_0$, where m_0 is the rest mass of an electron. Similar analysis can yield $m^* = 0.16m_0$ in a n-type WSe₂.

After extracting the effective mass, the quantum scattering time τ_q and quantum mobility μ_q can be accurately determined from the Dingle factor, where $\lambda_D = 2\pi^2 k_B m^* T_D / \hbar e B$. T_D is the Dingle temperature, given by $T_D = \hbar / 2\pi k_B \tau_q$. By plotting $\ln[\Delta R(B, T) B \sinh \lambda(T)]$ as a function of $1/B$, the slope of the linear fitting curves (shown in figure 3(d)) will yield T_D . At $T=2$ K, the fitting results in the Dingle temperature $T_D = 4.5$ K. The corresponding hole quantum scattering time $\tau_q = 269$ fs and the quantum mobility $\mu_q = e\tau_q / m^* = 1100$ cm²/Vs in p-type WSe₂. For n-type WSe₂, $\tau_q = 404$ fs and $\mu_q = 4400$ cm²/V s at $V_g=50$ V. For both of p-type and n-type samples, μ_q is slightly smaller than the corresponding Hall mobility,

since the quantum scattering time is shorter than the transport scattering time ($\tau_q < \tau_t$). This result indicates that the dominant scattering in few-layer WSe₂ is due to the long-range scattering caused by charge impurities [17]. By further reducing interfacial impurities or under sufficiently high magnetic fields, the sample quality should be ready for the exploration of quantum Hall and other quantum phenomena in TMDCs [34].

By comparing the carrier density measured by Hall effects with carrier density obtained from oscillation periods, we find that the n-type and p-type few-layer WSe₂ show different behaviors in valley degeneracy. Figure 4(e) shows the SdH oscillations of an n-type few-layer WSe₂ sample under magnetic fields of up to 14 T. The oscillations can be observed more clearly in figure 4(f) by plotting the numerical derivative dR/dB as a function of $1/B$. Fourier transformation of the oscillatory component reveals that, besides the first harmonic at $B_F=20$ T, a second harmonic appears near $B_F=40$ T. This second peak indicates the small spin-valley splitting between the Q-valleys along ΓK . The carrier density participating in the SdH oscillations, according to $n_s = g_s g_v e B_F / h$ ($g_s = 2$ for the spin degeneracy, and $g_v = 6$ for the Q-valley degeneracy), is approximately $5.8 \times 10^{12} \text{ cm}^{-2}$, which is in good agreement with the density ($6.0 \times 10^{12} \text{ cm}^{-2}$) measured by Hall effects. This further confirms that in few-layer WSe₂ [36] the conduction band bottom is located at the six-fold Q-valleys. For p-type few-layer WSe₂, the valance band top is located at the Γ -valley with $g_s = 2$ and $g_v = 1$. By considering the degeneracy in the Γ -valley, the calculated carrier density participating oscillations is $n_s = 2.8 \times 10^{12} \text{ cm}^{-2}$ at $V_g=-60$ V for p-type WSe₂, which is consistent with the corresponding carrier density measured by Hall effects ($2.7 \times 10^{12} \text{ cm}^{-2}$).

Conclusion

In summary, we have demonstrated a simple and effective approach for fabricating high-mobility atomically thin TMDC field-effect devices. High-quality low-temperature Ohmic contacts have been achieved via a selective etching process. We have found that clean interfaces and very low contact resistance realized in the h-BN/TMDC/h-BN encapsulation structures are critical in detecting the intrinsic transport properties of ultrathin TMDCs. Few-layer TMDC devices exhibit ultrahigh field-effect mobility at low temperatures, as well as clear quantum oscillations in intermedium magnetic field. The experimental results presented in this work pave the way for improving the quality of atomically thin TMDC devices and for exploring their quantum transport phenomena.

Methods

The h-BN encapsulated TMDC devices are fabricated by a dry transfer technique in an inert environment of argon or nitrogen. In a typical process, atomically thin TMDC sheets are mechanically exfoliated on SiO₂/Si substrates. The layer number of TMDC is determined by optical contrast, photoluminescence, and atomic force microscopy. Ultrathin h-BN sheets are exfoliated on a glass-supported PMMA film. We use a large h-BN sheet to pick up TMDC flakes through van der Waals interactions. The h-BN/TMDC stacks are then aligned to another h-BN thin sheet that had been previously exfoliated on SiO₂/Si substrates under an optical microscope. The PMMA-supported h-BN/TMDC is then transferred to the bottom h-BN to form a h-BN/TMDC/h-BN sandwich structure. PMMA is later removed by acetone. The final device structures are annealed under Ar/H₂ at 400 °C to remove small bubbles. To fabricate the metal contacts, the h-BN encapsulated TMDC is first patterned by standard e-beam lithography, and the top h-BN is etched by O₂ plasma via reaction-ion etching. The flow rate of O₂ is 40

sccm. The RF power is 200 W. Under this condition, the etching rate is about 10 nm/min for h-BN and 1 nm/min for TMDCs. For thick h-BN (>20 nm), the top h-BN can be initially rapidly etched by O₂ (4 sccm) mixed with CHF₃ (40 sccm) under a RF power of 200 W (the etching rate for h-BN in this recipe is about 100 nm/min) and then precisely etched by O₂ plasma only. Since the O₂ plasma etching rate for TMDC is low, the control of the etching process is not difficult. To guarantee the conducting channels are fully encapsulated by h-BN, a small overlap between the metal electrodes and the top h-BN is made by the second e-beam lithography for electrode patterning. Then, standard e-beam evaporation of Ti/Au (5 nm/80 nm) for n-type devices or Pd/Au (20 nm/80 nm) for p-type devices is carried out to deposit the electrodes on the etched patterns. To remove potential residues from PMMA, the samples are cleaned by O₂ plasma (8 s at 100 W) before metal electrode deposition. Characterization of electrical transport properties is conducted at cryostat temperatures, and the two-terminal I–V curves are measured by a Keithley 6430 instrument. Other transport data are collected by standard lock-in amplifier techniques.

Acknowledgement

The authors acknowledge the financial support provided by the Research Grants Council of Hong Kong (Project Nos. 16302215, HKU9/CRF/13G, 604112, and N_HKUST613/12) and the technical support provided by the Raith-HKUST Nanotechnology Laboratory for the electron-beam lithography facility at MCPF. F.Z. is supported by UT Dallas research enhancement funds, and thanks Gui-Bin Liu for helpful discussions.

Additional information

Supporting information is available.

Competing financial interests

The authors declare no competing financial interests.

Author contributions

S.G.X. and H.H.L. grew the WSe₂, MoSe₂ and MoTe₂ bulk crystal. S.G.X. and H.H.L. fabricated WSe₂ devices. Z.F.W. fabricated MoS₂ and WS₂ devices. S.G.X. fabricated MoSe₂ and MoTe₂ devices. S.G.X., Z.F.W., H.H.L. and Y.H. performed and analyzed the measurements under supervision of N.W.. S.G.X. and Y.H. performed the high magnetic field measurements with the help of J.Y.S. and R.L.. S.G.X., Z.F.W., F.Z., and N.W. analyze the quantum transport data. Other authors provided technical assistance on sample preparations and measurements and discussed on the paper. S.G.X. and N.W. wrote the paper with input from all authors.

References

- [1] Srivastava A, Sidler M, Allain A V, Lembke D S, Kis A and Imamoglu A 2015 Valley Zeeman effect in elementary optical excitations of monolayer WSe₂ *Nat Phys* **11** 141-7
- [2] Aivazian G, Gong Z, Jones A M, Chu R-L, Yan J, Mandrus D G, Zhang C, Cobden D, Yao W and Xu X 2015 Magnetic control of valley pseudospin in monolayer WSe₂ *Nat Phys* **11** 148-52
- [3] Mak K F, McGill K L, Park J and McEuen P L 2014 The valley Hall effect in MoS₂ transistors *Science* **344** 1489-92
- [4] Radisavljevic B, Radenovic A, Brivio J, Giacometti V and Kis A 2011 Single-layer MoS₂ transistors *Nat Nano* **6** 147-50
- [5] Lopez-Sanchez O, Lembke D, Kayci M, Radenovic A and Kis A 2013 Ultrasensitive photodetectors based on monolayer MoS₂ *Nat Nano* **8** 497-501
- [6] Wang Q H, Kalantar-Zadeh K, Kis A, Coleman J N and Strano M S 2012 Electronics and optoelectronics of two-dimensional transition metal dichalcogenides *Nat Nano* **7**

699-712

- [7] Splendiani A, Sun L, Zhang Y, Li T, Kim J, Chim C-Y, Galli G and Wang F 2010 Emerging Photoluminescence in Monolayer MoS₂ *Nano Lett.* **10** 1271-5
- [8] Zeng H, Dai J, Yao W, Xiao D and Cui X 2012 Valley polarization in MoS₂ monolayers by optical pumping *Nat Nano* **7** 490-3
- [9] Yuan H, Bahramy M S, Morimoto K, Wu S, Nomura K, Yang B-J, Shimotani H, Suzuki R, Toh M, Kloc C, Xu X, Arita R, Nagaosa N and Iwasa Y 2013 Zeeman-type spin splitting controlled by an electric field *Nat Phys* **9** 563-9
- [10] Chuang H-J, Tan X, Ghimire N J, Perera M M, Chamlagain B, Cheng M M-C, Yan J, Mandrus D, Tománek D and Zhou Z 2014 High Mobility WSe₂ p- and n-Type Field-Effect Transistors Contacted by Highly Doped Graphene for Low-Resistance Contacts *Nano Lett.* **14** 3594-601
- [11] Fang H, Chuang S, Chang T C, Takei K, Takahashi T and Javey A 2012 High-Performance Single Layered WSe₂ p-FETs with Chemically Doped Contacts *Nano Lett.* **12** 3788-92
- [12] Gong C, Colombo L, Wallace R M and Cho K 2014 The Unusual Mechanism of Partial Fermi Level Pinning at Metal–MoS₂ Interfaces *Nano Lett.* **14** 1714-20
- [13] Das S, Chen H-Y, Penumatcha A V and Appenzeller J 2013 High Performance Multilayer MoS₂ Transistors with Scandium Contacts *Nano Lett.* **13** 100-5
- [14] Baugher B W H, Churchill H O H, Yang Y and Jarillo-Herrero P 2013 Intrinsic Electronic Transport Properties of High-Quality Monolayer and Bilayer MoS₂ *Nano Lett.* **13** 4212-6
- [15] Kappera R, Voiry D, Yalcin S E, Branch B, Gupta G, Mohite A D and Chhowalla M 2014 Phase-engineered low-resistance contacts for ultrathin MoS₂ transistors *Nat Mater* **13** 1128-34
- [16] Liu W, Kang J, Sarkar D, Khatami Y, Jena D and Banerjee K 2013 Role of Metal Contacts in Designing High-Performance Monolayer n-Type WSe₂ Field Effect Transistors *Nano Lett.* **13** 1983-90
- [17] Cui X, Lee G-H, Kim Y D, Arefe G, Huang P Y, Lee C-H, Chenet D A, Zhang X, Wang

- L, Ye F, Pizzocchero F, Jessen B S, Watanabe K, Taniguchi T, Muller D A, Low T, Kim P and Hone J 2015 Multi-terminal transport measurements of MoS₂ using a van der Waals heterostructure device platform *Nat Nano* **10** 534-40
- [18] Cao Y, Mishchenko A, Yu G L, Khestanova E, Rooney A P, Prestat E, Kretinin A V, Blake P, Shalom M B, Woods C, Chapman J, Balakrishnan G, Grigorieva I V, Novoselov K S, Piot B A, Potemski M, Watanabe K, Taniguchi T, Haigh S J, Geim A K and Gorbachev R V 2015 Quality Heterostructures from Two-Dimensional Crystals Unstable in Air by Their Assembly in Inert Atmosphere *Nano Lett.* **15** 4914-21
- [19] Dean C R, Young A F, Meric I, Lee C, Wang L, Sorgenfrei S, Watanabe K, Taniguchi T, Kim P, Shepard K L and Hone J 2010 Boron nitride substrates for high-quality graphene electronics *Nat Nano* **5** 722-6
- [20] Wang L, Meric I, Huang P Y, Gao Q, Gao Y, Tran H, Taniguchi T, Watanabe K, Campos L M, Muller D A, Guo J, Kim P, Hone J, Shepard K L and Dean C R 2013 One-Dimensional Electrical Contact to a Two-Dimensional Material *Science* **342** 614-7
- [21] Solanki G K, Gujarathi D N, Deshpande M P, Lakshminarayana D and Agarwal M K 2008 Transport property measurements in tungsten sulphoselenide single crystals grown by a CVT technique *Cryst. Res. Technol.* **43** 179-85
- [22] Yu L, Lee Y-H, Ling X, Santos E J G, Shin Y C, Lin Y, Dubey M, Kaxiras E, Kong J, Wang H and Palacios T 2014 Graphene/MoS₂ Hybrid Technology for Large-Scale Two-Dimensional Electronics *Nano Lett.* **14** 3055-63
- [23] Lee G-H, Yu Y-J, Cui X, Petrone N, Lee C-H, Choi M S, Lee D-Y, Lee C, Yoo W J, Watanabe K, Taniguchi T, Nuckolls C, Kim P and Hone J 2013 Flexible and Transparent MoS₂ Field-Effect Transistors on Hexagonal Boron Nitride-Graphene Heterostructures *ACS Nano* **7** 7931-6
- [24] Roy T, Tosun M, Kang J S, Sachid A B, Desai S B, Hettick M, Hu C C and Javey A 2014 Field-Effect Transistors Built from All Two-Dimensional Material Components *ACS Nano* **8** 6259-64
- [25] Allain A and Kis A 2014 Electron and Hole Mobilities in Single-Layer WSe₂ *ACS Nano* **8** 7180-5

- [26] Wang J I J, Yang Y, Chen Y-A, Watanabe K, Taniguchi T, Churchill H O H and Jarillo-Herrero P 2015 Electronic Transport of Encapsulated Graphene and WSe₂ Devices Fabricated by Pick-up of Prepatterned hBN *Nano Lett.* **15** 1898-903
- [27] Leong W S, Luo X, Li Y, Khoo K H, Quek S Y and Thong J T L 2015 Low Resistance Metal Contacts to MoS₂ Devices with Nickel-Etched-Graphene Electrodes *ACS Nano* **9** 869-77
- [28] Buscema M, Steele G, van der Zant H J and Castellanos-Gomez A 2014 The effect of the substrate on the Raman and photoluminescence emission of single-layer MoS₂ *Nano Res.* **7** 561-71
- [29] Fuhrer M S and Hone J 2013 Measurement of mobility in dual-gated MoS₂ transistors *Nat Nano* **8** 146-7
- [30] Radisavljevic B and Kis A 2013 Mobility engineering and a metal–insulator transition in monolayer MoS₂ *Nat Mater* **12** 815-20
- [31] Chen B, Sahin H, Suslu A, Ding L, Bertoni M I, Peeters F M and Tongay S 2015 Environmental Changes in MoTe₂ Excitonic Dynamics by Defects-Activated Molecular Interaction *ACS Nano* **9** 5326-32
- [32] Chamlagain B, Li Q, Ghimire N J, Chuang H-J, Perera M M, Tu H, Xu Y, Pan M, Xiaio D, Yan J, Mandrus D and Zhou Z 2014 Mobility Improvement and Temperature Dependence in MoSe₂ Field-Effect Transistors on Parylene-C Substrate *ACS Nano* **8** 5079-88
- [33] Li L, Yu Y, Ye G J, Ge Q, Ou X, Wu H, Feng D, Chen X H and Zhang Y 2014 Black phosphorus field-effect transistors *Nat Nano* **9** 372-7
- [34] Li X, Zhang F and Niu Q 2013 Unconventional Quantum Hall Effect and Tunable Spin Hall Effect in Dirac Materials: Application to an Isolated MoS₂ Trilayer *Phys. Rev. Lett.* **110** 066803
- [35] Tayari V, Hemsworth N, Fakih I, Favron A, Gaufres E, Gervais G, Martel R and Szkopek T 2015 Two-dimensional magnetotransport in a black phosphorus naked quantum well *Nat Commun* **6** 7702
- [36] Zeng H, Liu G-B, Dai J, Yan Y, Zhu B, He R, Xie L, Xu S, Chen X, Yao W and Cui X

2013 Optical signature of symmetry variations and spin-valley coupling in atomically thin tungsten dichalcogenides *Sci. Rep.* **3** 1608

Figures and Legends

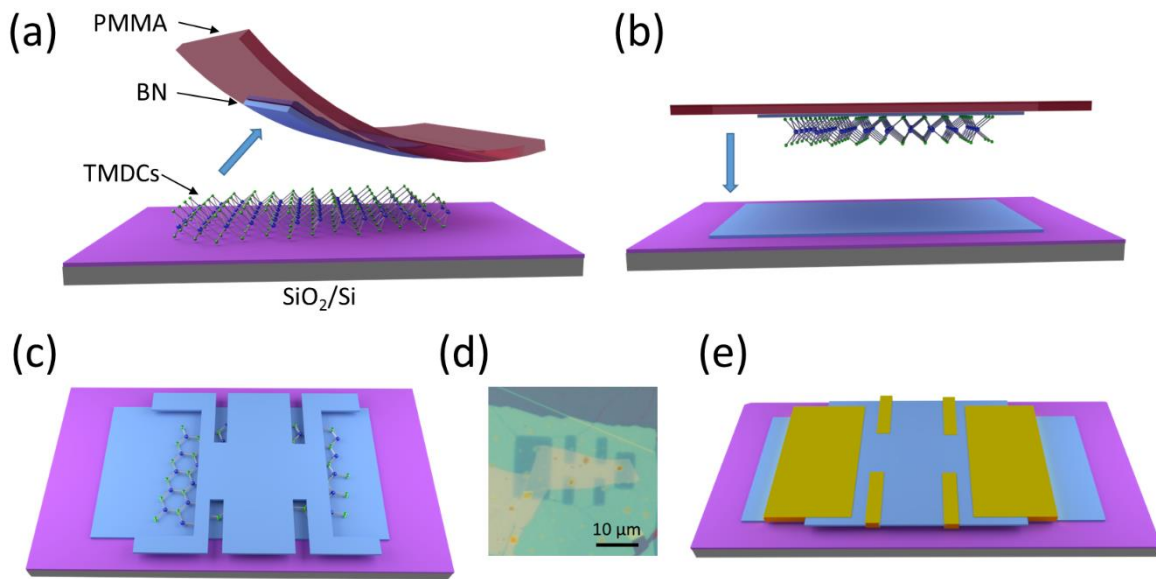


Figure 1. Fabrication flow of h-BN encapsulated few-layer TMDC devices. (a), Schematic of TMDC picked up by a h-BN flake on PMMA. (b), TMDC/h-BN is transferred to the bottom h-BN to form a h-BN/TMDC/h-BN sandwich structure. (c), Contact regions with a Hall bar pattern are etched by O₂ plasma. (d), Optical image of the device after O₂ plasma etching. (e), Final device obtained after deposition of metal electrodes.

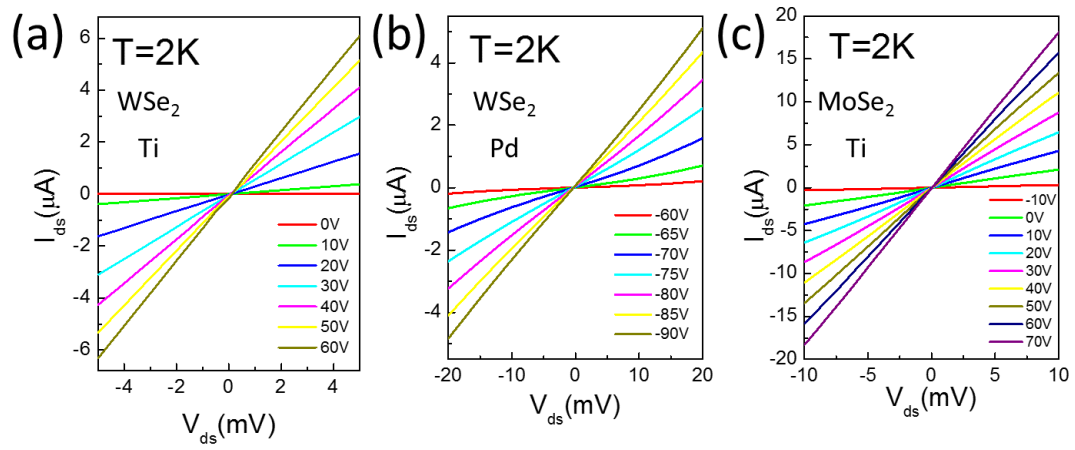


Figure 2. Performance of the metal electrode contact in the h-BN/TMDC/h-BN van der Waals structures. (a) –(c), I_{ds} - V_{ds} characteristics obtained by a two-terminal configuration at $T=2\text{K}$ for (a) n-type WSe_2 (b) p-type WSe_2 and (c) n-type MoSe_2 . Linear I_{ds} - V_{ds} curves are observed at various back gates, indicating Ohmic contacts.

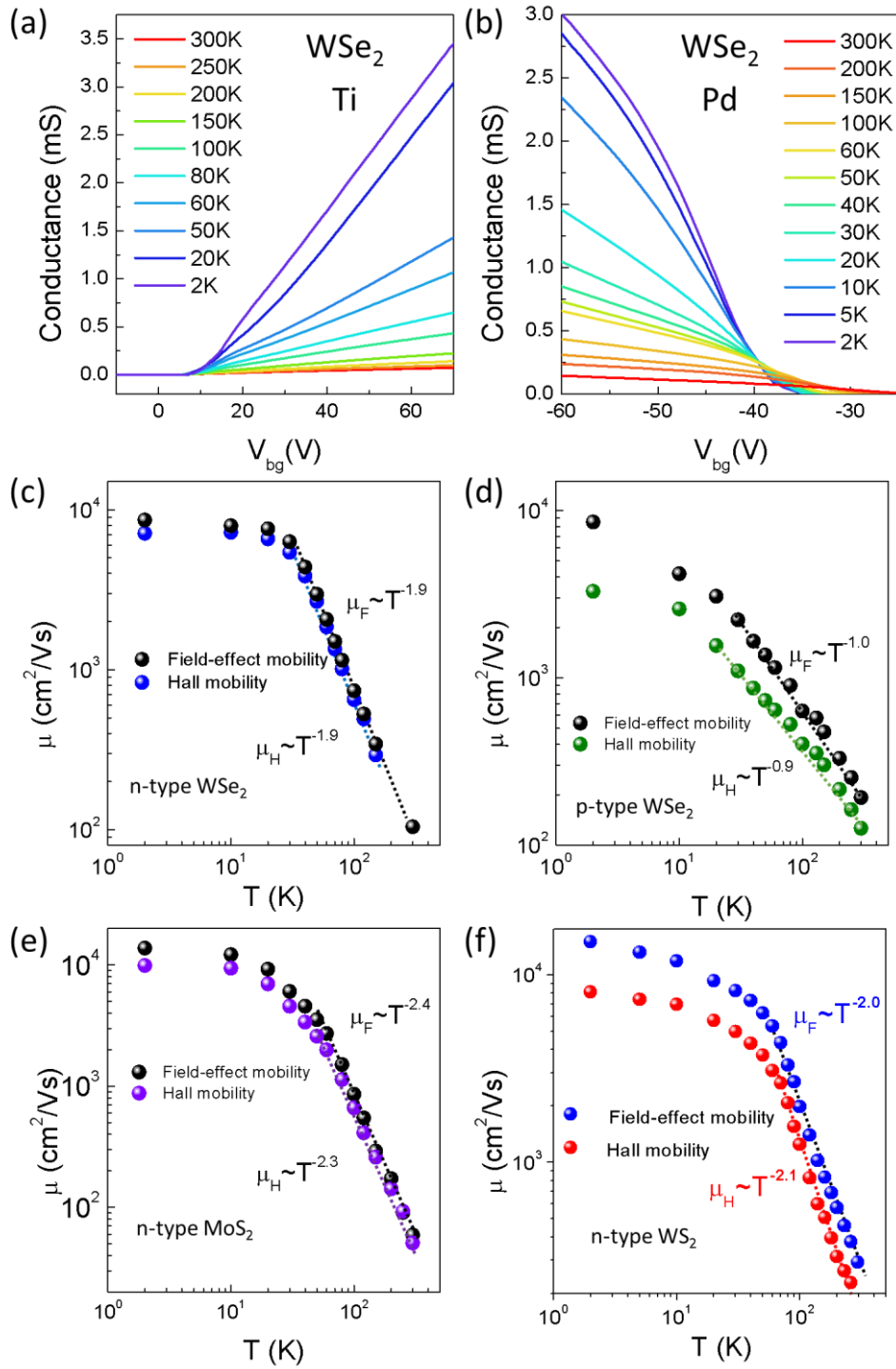


Figure 3. Temperature-dependent conductance and mobility engineering. (a), (b), Four-terminal conductance plotted as a function of back gate voltage at various temperatures: (a) n-type WSe₂ with Ti as contact metal; (b) p-type WSe₂ with Pd as contact metal. (c)-(f), Field-effect and Hall mobilities at various temperatures for few-layer (c) n-type WSe₂, (d) p-type WSe₂, (e) n-type MoS₂, and (f) n-type WS₂. Linear fittings were used in the phonon-limited region to extract γ .

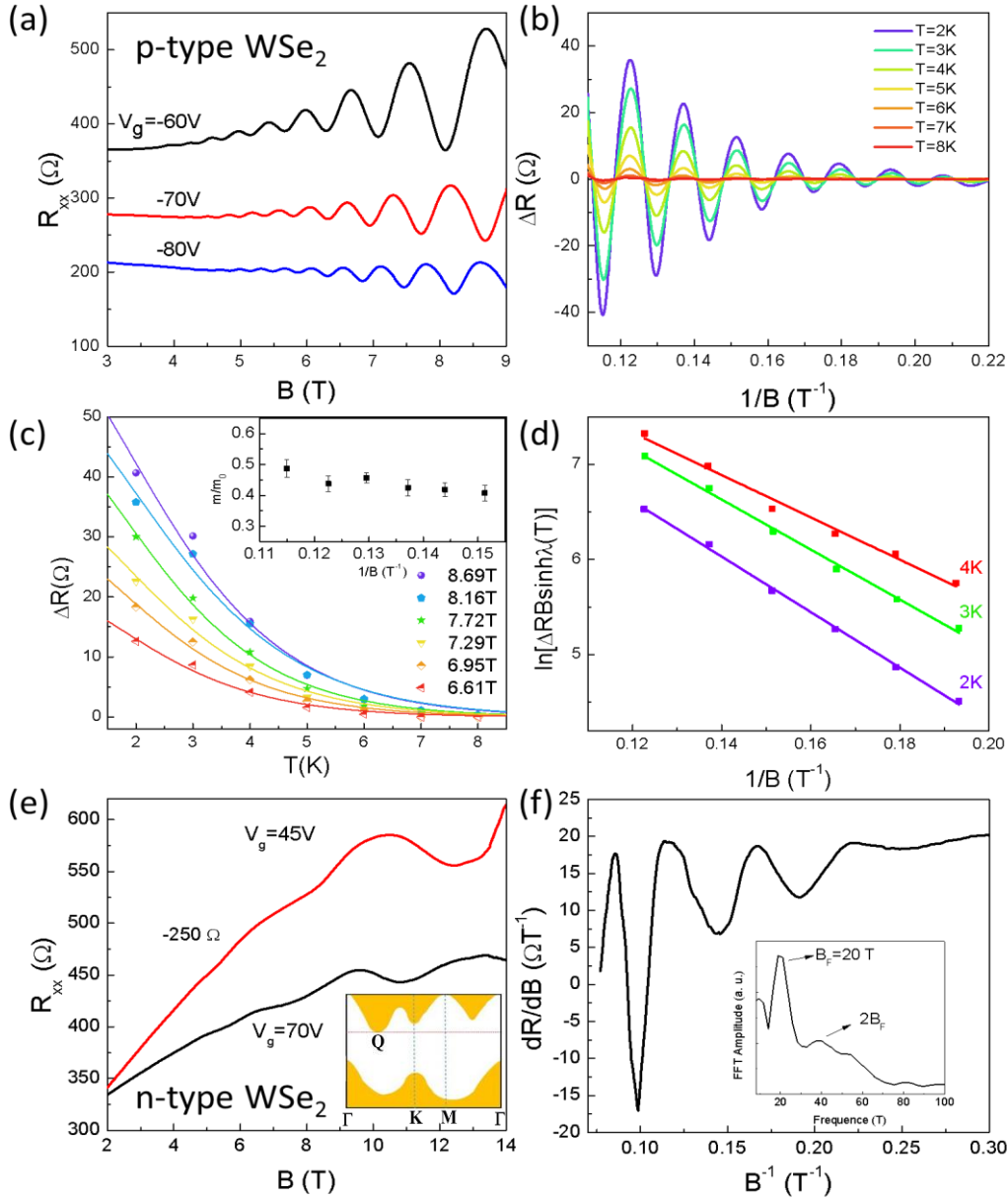


Figure 4. Shubnikov–de Haas oscillations in h-BN encapsulated few-layer TMDCs. (a), Longitudinal resistance plotted as a function of magnetic field at various voltages in a few-layer p-type WSe₂ sample. (b), SdH oscillation as a function of $1/B$ measured at different temperatures with V_g fixed at -70 V. To obtain ΔR , the magnetoresistance R_{xx} is subtracted by a smooth background. (c), SdH oscillation amplitudes as a function of temperature at different magnetic fields. The solid lines are the fitting results using the Lifshitz-Kosevich formula. The inset shows the fitting results of the cyclotron effective mass. (d), Dingle plots of $\ln[\Delta R B T / \sinh(\lambda T)]$ as a function of $1/B$ at different temperatures. Quantum scattering time and quantum mobility can be extracted from the linear fittings. (e), SdH oscillations in a few-layer n-type WSe₂ sample. The inset is the schematic band structure of few-layer WSe₂. (f), Numerical derivative dR/dB plotted as a function of $1/B$ for data at $V_g=70$ V in (e). The inset reveals the fast Fourier transformation result of the oscillations.

	μ_{Field} (cm ² /V s)	μ_{Hall} (cm ² /V s)	Carrier density (cm ⁻²)	γ_{Field}	γ_{Hall}	Contact resistance (k Ω · μ m)
MoS ₂	14,000	9,900	8.8×10 ¹²	2.4	2.3	0.5
WSe ₂	8,600	7,100	5.1×10 ¹²	1.9	1.9	0.2
WS ₂	16,000	8,000	5.3×10 ¹²	2.0	2.1	0.5
MoSe ₂	4,400	2,100	1.3×10 ¹³	1.9	2.1	0.3
MoTe ₂	2,300	600	6.2×10 ¹²	1.5	1.3	12
P-type WSe ₂	8,550	3,300	4.3×10 ¹²	1.0	0.9	4.8

Table 1 | Summary of the transport performance of the h-BN encapsulated few-layer TMDCs characterized at T=2 K.

Supplementary Material for

Universal low-temperature Ohmic contacts for quantum transport in transition metal dichalcogenides

Shuigang Xu^{1†}, Zefei Wu^{1†}, Huanhuan Lu^{1†}, Yu Han¹, Gen Long¹, Xiaolong Chen¹, Tianyi Han¹, Weiguang Ye¹, Yingying Wu¹, Jiangxiazhi Lin¹, Junying Shen¹, Yuan Cai¹, Yuheng He¹, Fan Zhang², Rolf Lortz¹, Chun Cheng³, Ning Wang^{1}*

¹Department of Physics and Center for 1D/2D Quantum Materials, the Hong Kong University of Science and Technology, Clear Water Bay, Hong Kong, China

²Department of Physics, the University of Texas at Dallas, Richardson, Texas 75080, USA

³Department of Materials Science and Engineering and Shenzhen Key Laboratory of Nanoimprint Technology, South University of Science and Technology, Shenzhen 518055, China

[†]These authors contributed equally

**Corresponding author: phwang@ust.hk*

1. Device fabrication

Figure S1 shows the fabrication of the h-BN/TMDC/h-BN device by the dry transferring method followed by a chemical etching processes and electron beam evaporation. A WSe₂ flake is used for making the device shown in Figure S1.

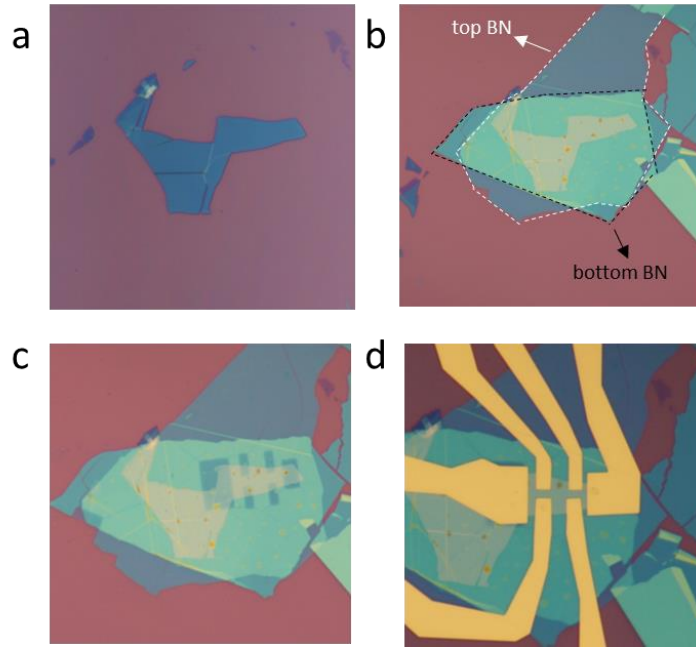


Figure S1: Optical images of TMDC device fabrication process. **a**, Few-layer WSe₂ flakes exfoliated on a SiO₂/Si substrate. **b**, A WSe₂ flake picked up by a h-BN sheet and transferred to another h-BN sheet. **c**, Hall bar pattern generated by standard e-beam lithography techniques and etched by the reactive ion etching process. **d**, The metal electrodes deposited on the sample via e-beam evaporation techniques.

2. Hysteresis effects

Figure S2 shows the positive and negative sweeps of the $G-V_g$ curves which are perfectly overlapped to each other, indicating that there is no hysteresis effect. The charge trapping effects have been effectively suppressed in these h-BN encapsulated structures.

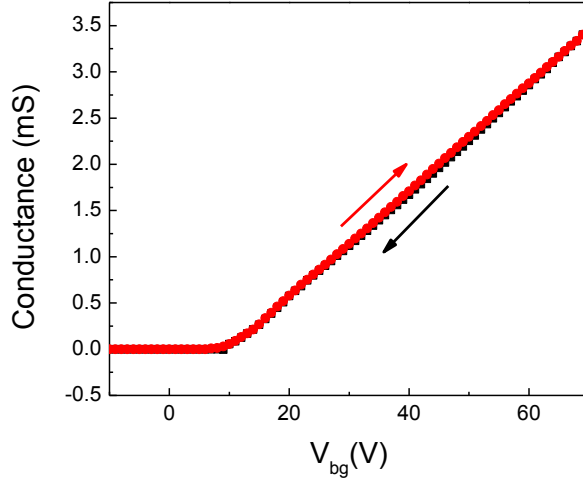


Figure S2: The positive and negative sweeps of the conductance as a function of gate voltages at 2 K.

3. Ohmic contacts

Ohmic contacts have been achieved in all samples in this study. Linear I_{ds} - V_{ds} curves are observed at various temperatures as shown in Figure S3. To investigate the contact barriers in our devices, sample conductance is measured as a function of V_g for different excitation voltages through a four-terminal configuration (see Figure S3c). All the curves coincide to a single curve, indicating that the injection of charge carriers is independent of the excitation voltages. Thus, the electrical properties of the channel materials are truly reflected by the transport data. Similar linear I_{ds} - V_{ds} curves are observed in other materials as shown in Figure S4.

The barrier free contacts in our samples have been further confirmed using the Arrhenius plot¹ of $\ln(I_{ds}/T^{3/2})$ versus $1000/T$. The Arrhenius plots of temperature dependent transport of n-type WSe₂ and MoSe₂ are shown in Figure S5 with $I_{ds}=0.1$ V. All the fitting curves at various gate voltages have similar positive slopes, which indicate that the contact barriers are almost

independent on the back gates voltages. This kind of contacts is very different from the graphene/MoS₂ contact^{2,3}.

We find that the h-BN encapsulated structure is very critical for the formation of reliable low-temperature Ohmic contacts. Without using the bottom or top h-BN, all TMDC devices show very poor contacts, which can be found from the I_{ds} - V_{ds} curves obtained at room- and low-temperatures. By applying the controlled etching process (using the same contact metals (Ti/Au)), we fabricated two kinds of devices to demonstrate the functions of h-BN: Device-A without bottom h-BN and Device-B without top h-BN. Device-A displays serious non-linear behaviors at room- and low-temperatures as shown in Figure S6, indicating the impurities induced gap states at the interface between SiO₂ and TMDC, resulting in poor contacts. Device-B has a better performance, but asymmetrical I_{ds} - V_{ds} curves at low-temperatures, as shown in Figure S7e, indicating that a small Schottky barrier should occur at the contacts. Therefore, we believe that the clean surface realized by h-BN encapsulation plays an important role in achieving low-temperature Ohmic contacts.

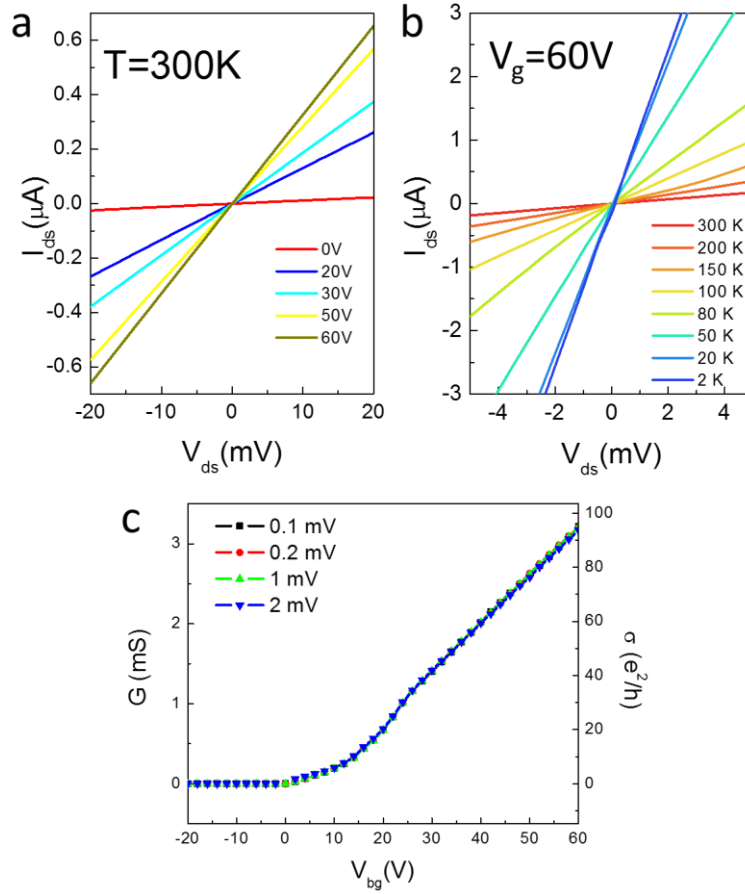


Figure S3: Contact performance at different temperatures. **a**, I_{ds} - V_{ds} characteristics obtained by a two-terminal configuration at room temperature. **b**, Two-terminal output curves at various temperatures with back gate voltages kept at 60 V. Ohmic contacts are observed in a wide range of temperatures. **c**, Conductance plotted as a function of back gate voltages with different excitation voltages at 2 K.

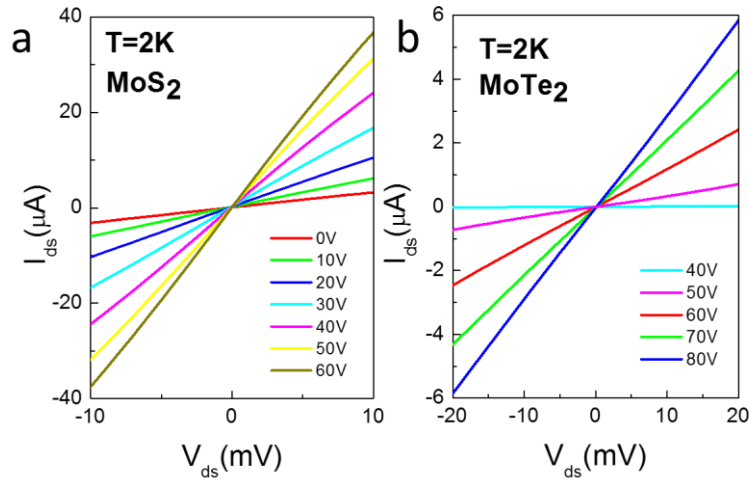


Figure S4: Two-terminal I_{ds} - V_{ds} characteristics at $T=2$ K for n-type MoS_2 and MoTe_2 devices.

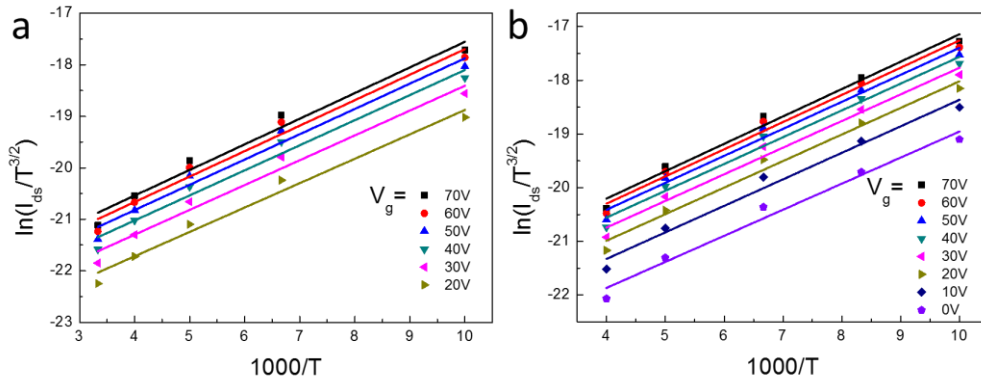


Figure S5: Arrhenius plots of $\ln(I_{ds}/T^{3/2})$ versus $1000/T$ at various back gate voltages for WSe_2 (a) and MoSe_2 (b). The positive slope indicates zero barrier in the contacts.

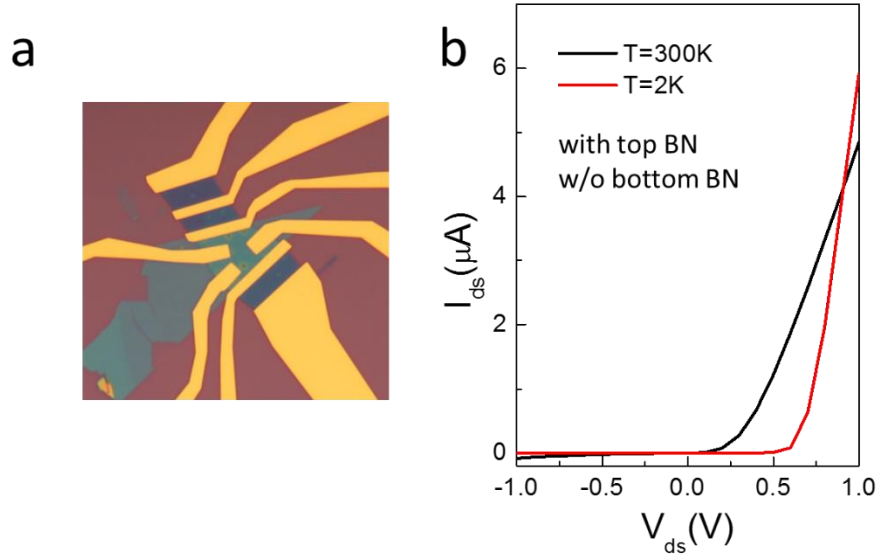


Figure S6: Control experiments and the output characteristics (I_{ds} - V_{ds} curves) of few-layer WSe₂ without bottom h-BN. **a, optical images of the device. **b**, I_{ds} - V_{ds} curves of the electrodes fabricated on the WSe₂ sample protected by a top h-BN.**

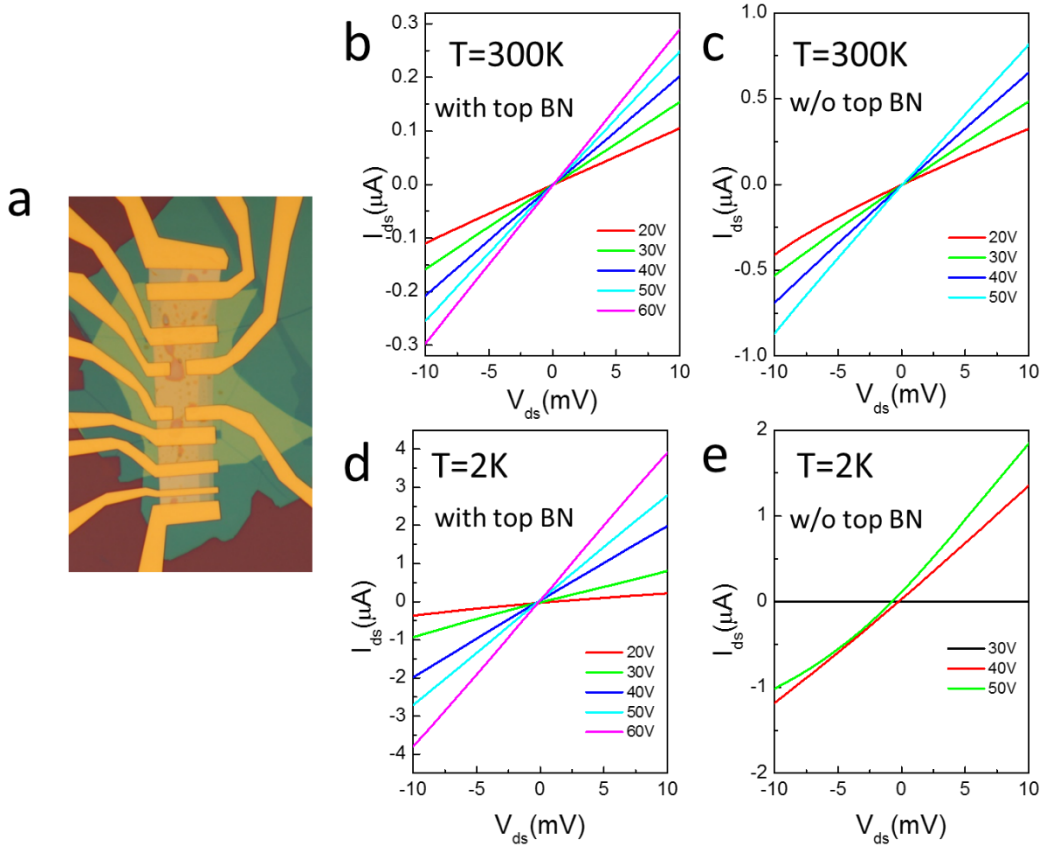


Figure S7: Control experiments and the output characteristics (I_{ds} - V_{ds} curves) of few-layer WSe₂ without a top h-BN. a, an optical image of the device. **b, d,** I_{ds} - V_{ds} curves of the electrodes fabricated on the WSe₂ protected by a top h-BN. **c, e,** I_{ds} - V_{ds} curves of the electrodes fabricated on the WSe₂ without top h-BN protection.

4. Temperature dependent conductance in other TMDCs.

Figure S8 shows temperature dependent conductance at different gate voltages for various TMDC samples. With Ti as the contact metal, all of the TMDCs show n-type behaviors, except the MoTe₂ devices at room temperature. Because MoTe₂ has more narrow bandgap than other TMDCs, the Schottky barrier for the hole injection in MoTe₂ is smaller. Therefore, we can observe the ambipolar effect in MoTe₂ at room temperature with the hole conducts at negative

gate voltages as shown in the inset of Figure S8c. The hole conduction dramatically decrease and are finally difficult to detect when the temperature goes down to cryogenic temperatures. This indicates at low temperature, thermal excitation energy becomes too small to overcome the Schottky barriers, which further limit the injection of holes.

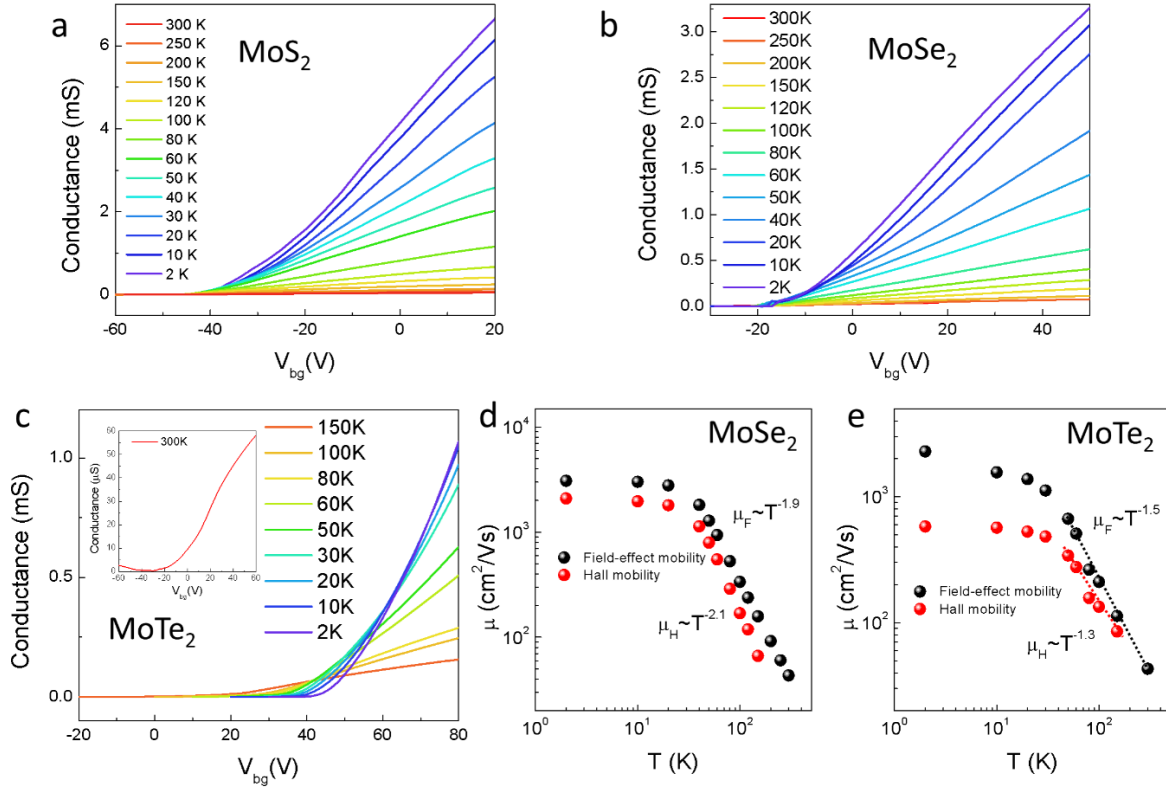


Figure S8: The conductance changes plotted as a function of back gate voltages measured by four-terminal configurations for a, MoS₂; b, MoSe₂; c, MoTe₂. d, e, temperature dependent field-effect and Hall mobility for (d) few-layer MoTe₂ devices and (e) few-layer MoSe₂ devices.

5. Low-temperature contact resistance

The contact resistance can be estimated by $R_c = R_{2p} - \frac{L_{tot}}{L_{in}} R_{4p}$, where R_{2p} is two-terminal resistance, R_{4p} is the four-terminal resistance, L_{tot} and L_{in} are the total and inner channel lengths,

respectively. R_c as a function of gate voltages at T=2 K are plotted in Figure S8 for different materials. The unit length contact resistance can be calculated as $R_c W/2$, considering the source and drain contributions. The results are summarized in Table 1.

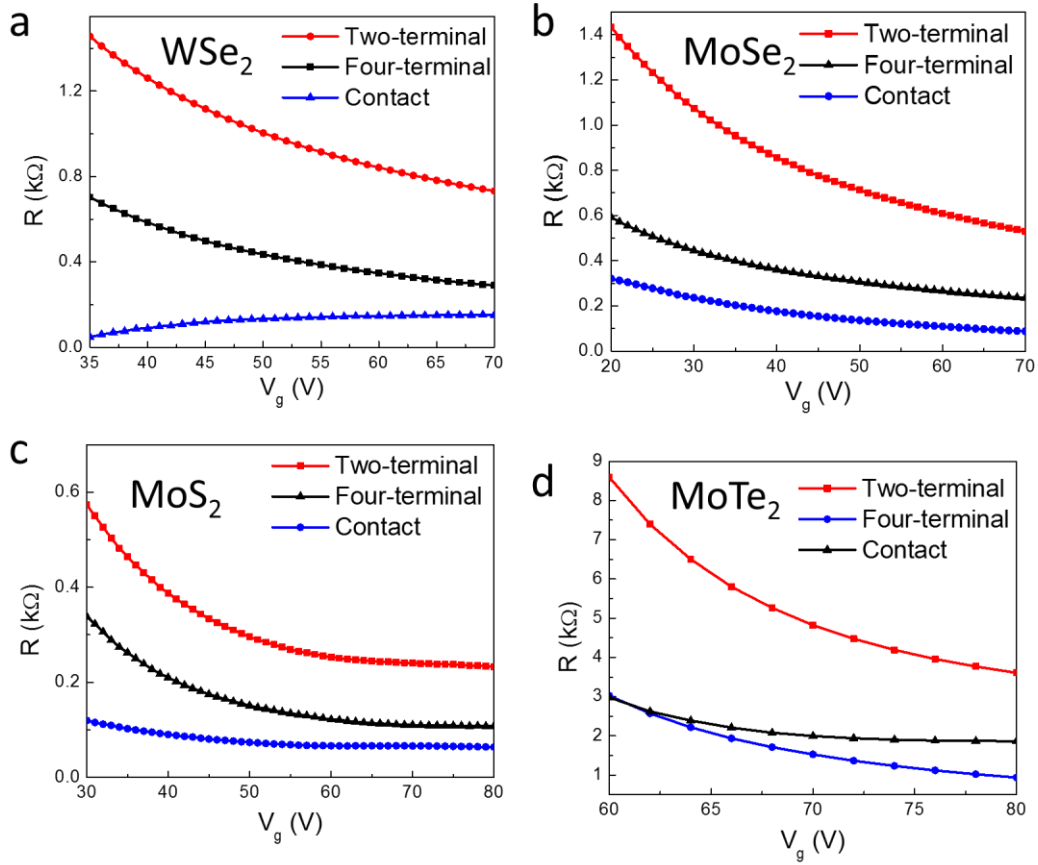


Figure S9: Gate voltages dependent contact resistance at T=2 K for various n-type devices: a, WSe₂; b, MoSe₂; c, MoS₂; d, MoTe₂.

6. Carrier density and gate capacitance determined by Hall effects

We use Hall effect data to determine the Hall mobility, density of charge carriers and gate capacitance. Figure S10a shows that the transverse Hall resistance R_{xy} of the device at different V_g . R_{xy} is linearly dependent on the magnetic field B . The Hall coefficient R_H is extracted from

the slope. Then the carrier density is calculated according to $n_{2D} = 1/R_H e$ and the Hall mobility is obtained by $\mu_H = \sigma/ne$. The variation of n_{2D} as a function of V_g is shown in Figure S10b. The data can be fitted by $n_{2D} = n_0 + C_g V_g/e$, whose slope yields $C_g = 1.14 \times 10^{-8}$ F/cm². This gate capacitance is used to calculate the field-effect mobility.

Figure S11 illustrates that the Hall mobility is dependent on the carrier density. The density dependence of the Hall mobility is due to the long-range Coulomb impurities in the samples. Increasing the carrier density enhances the screening of Coulomb potential, which results in an increase of the Hall mobility. The carrier density dependence of the Hall mobility leads to that the measured μ_H is smaller than μ_F . Because when we substitute $\sigma = ne\mu_H$ and $n = C_g(V_g - V_{th})/e$ into the definition of field-effect mobility $\mu_F = (d\sigma/dV_g)/C_g$, we will find $\mu_F = \mu_H + nd\mu_H/dn$. Therefore, μ_F will be larger than μ_H when $d\mu_H/dn > 0$.

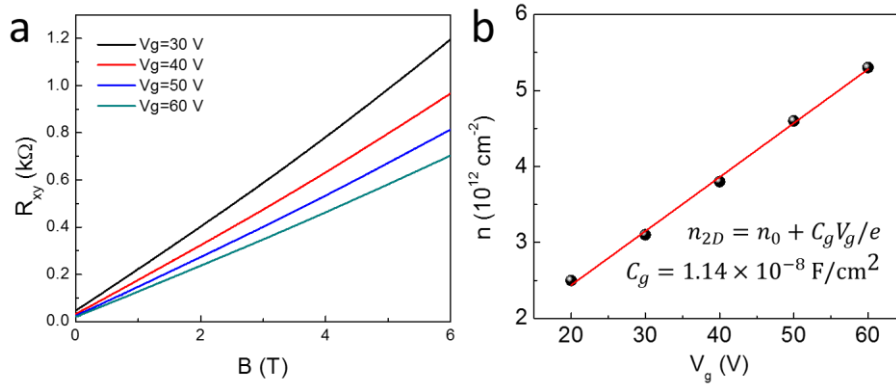


Figure S10: Capacitance extracted from Hall effect measurements. a, The Hall resistance plotted as a function of magnetic fields for different back gate voltages. **b**, The electron density extracted from the Hall coefficient R_H at different voltages.

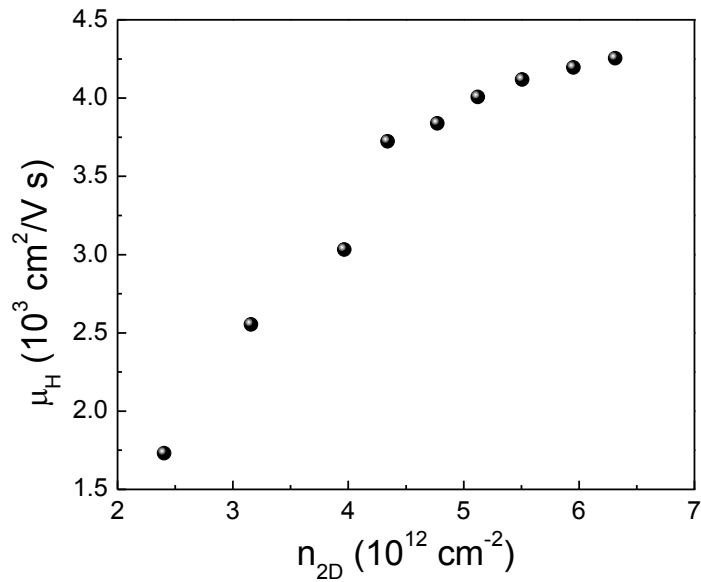


Figure S11: The carrier density dependence of the Hall mobility in a 5L WSe₂ sample.

7. Stability of h-BN encapsulated TMDC devices

The h-BN encapsulated devices can maintain their high performance after a long time storing in air. Figure S12 shows the mobility of a WSe₂ device is still over 8000 cm²/V s after 4 months. The slight shift of the threshold voltage may be due to the influence of the impurity levels in SiO₂.

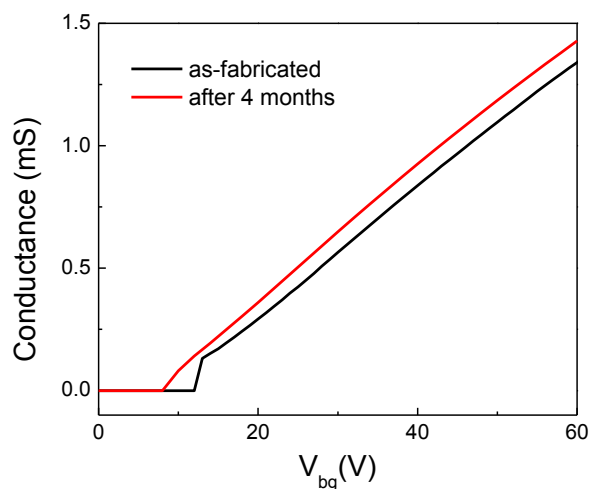


Figure S12: The changes of the electrical transport characteristics of a WSe₂ sample after storing in air for 4 months.

8. Transport behaviors of few-layer WSe₂ prepared on SiO₂/Si substrates

We have studied the transport behaviors of few-layer WSe₂ exfoliated on SiO₂/Si substrates. Two kinds of metal contacts, Ti/Au and Pd/Au have been used for comparison. As shown in Figure S13 and S14, both contacts show poor performance since large Schottky barriers formed at the interfaces between the electrodes and WSe₂. It is difficult to measure the conductance by four-terminal configurations or at low temperatures due to the large contact resistances. Figure S13 and S14 show the characteristics of Pd and Ti contacts (two-terminal configuration), respectively. For Pd contacts, the measured electron mobility is only 0.2 cm²/V s and hole mobility 0.04 cm²/V s. For Ti contacts, the hole mobility is 8.7 cm²/V s. Moreover, the devices prepared on SiO₂ show large hysteresis effects, indicating that there are lots of charge traps at the interface between SiO₂ and WSe₂.

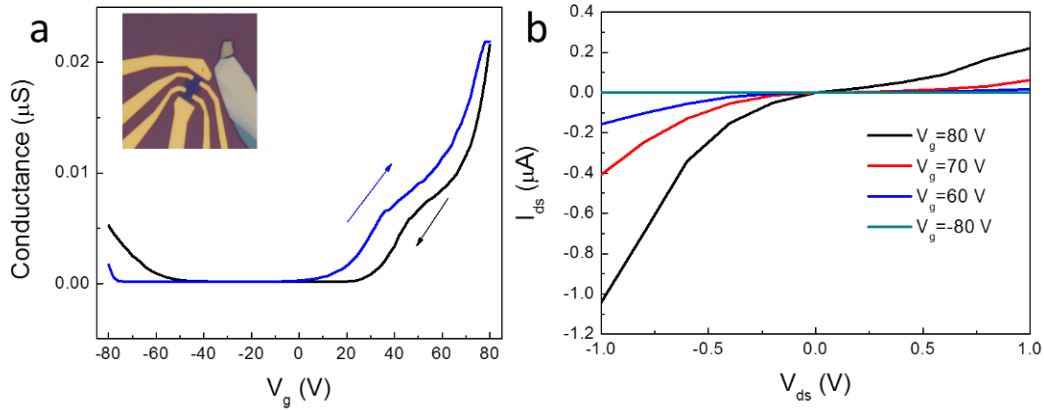


Figure S13: Transport behaviors of a few-layer WSe₂ sample prepared on a SiO₂/Si substrate with Pd/Au electrodes. a, Conductance measured as a function of gate voltages at room temperature. The inset is the optical image of the device. **b**, I_{ds} - V_{ds} curves measured at different gate voltages.

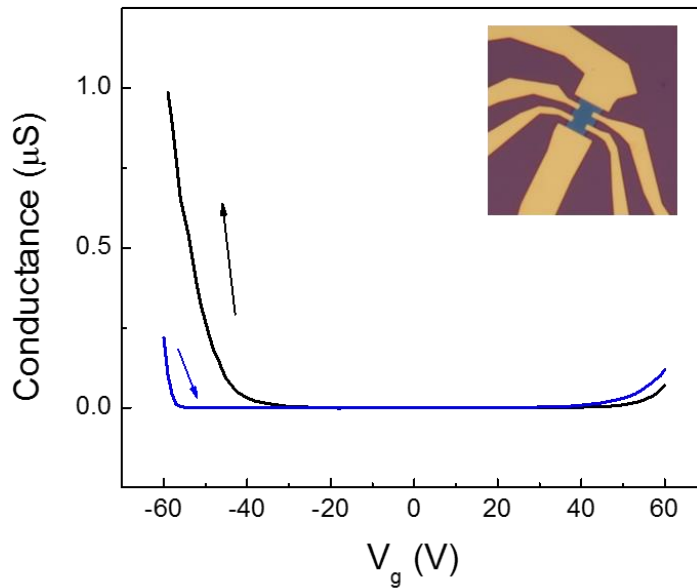


Figure S14: Room-temperature transport behaviors of a WSe₂ sample prepared on a SiO₂/Si substrate with Ti/Au contact.

9. Transport behaviors of h-BN encapsulated few-layer WSe₂ with edge contacts.

Although the one-dimensional edge contacts for h-BN encapsulated graphene⁴ show excellent electrical performance, the same fabrication did not produce satisfactory results for h-BN encapsulated few-layer WSe₂. To achieve the edge contacts, 4 sccm O₂ and 40 sccm CHF₃ were used. The inset in Figure S15 shows the Hall bar pattern after the etching process. Two kinds of electrodes, Ti/Au and Pd/Au have been tested as edge contacts. Although the edge contact does work, the performance are not good enough. As shown in Figure S15, the hole mobility obtained using Pd/Au edge contacts was about 5 cm²/V s. For Ti/Au edge contacts (Figure S16), we obtained the electron mobility of about 6.4 cm²/V s at $V_{ds} = 0.5$ V.

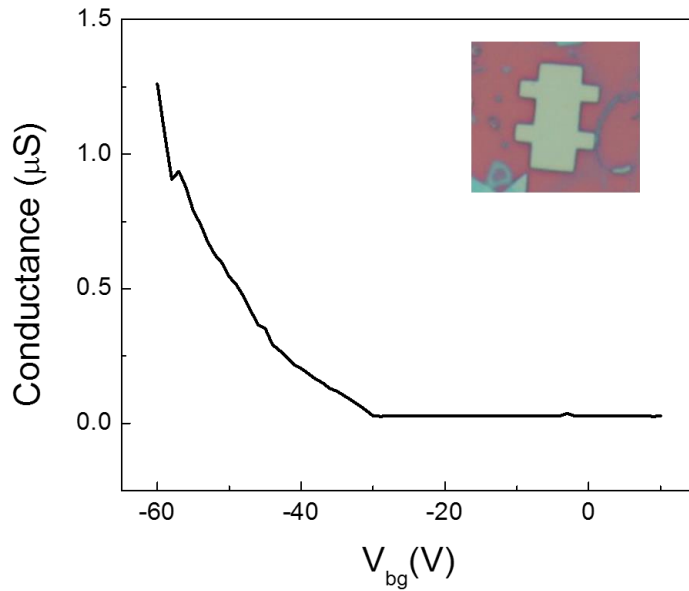


Figure S15: Transport behaviors of h-BN encapsulated WSe₂ measured with Pd/Au edge contacts at room-temperature.

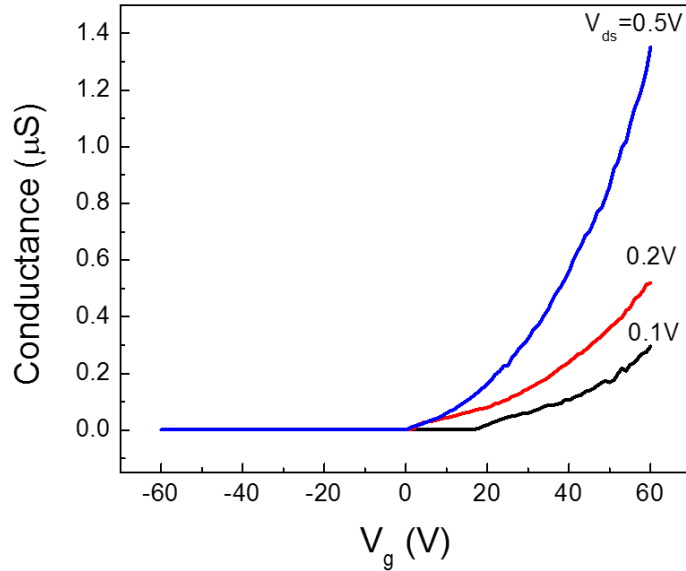


Figure S16: Transport behaviors of h-BN encapsulated WSe₂ measured with Ti/Au edge contacts at room-temperature. Excitation voltages of 0.1 V, 0.2 V and 0.5 V are used for the measurements.

10. Thickness determination by atomic force microscopy

We use AFM to identify the thickness of TMDC samples. The thickness of single layer WSe₂ is about 0.7 nm. Figure S17 shows AFM data for the 5L and 8L WSe₂ samples.

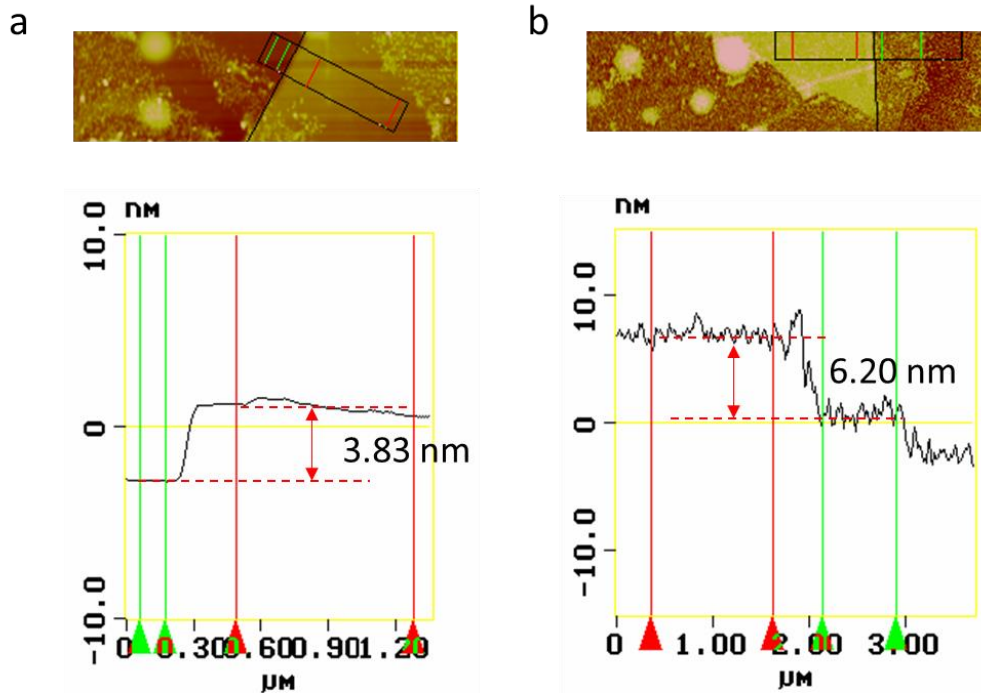


Figure S17: AFM results obtained from few-layer WSe₂ samples. a, 5L sample. b, 8L sample.

11. Optical characterization of few-layer WSe₂ and MoSe₂ samples

Figure S18 shows the photoluminescence (PL) and Raman scattering data taken from WSe₂ samples with different thicknesses. The wavelength of the excitation laser source is 514 nm. For PL, single layer WSe₂ exhibits a high intensity around 750 nm, indicating the direct band gap nature. For WSe₂ samples with thickness >2 layers, indirect gap inter-band transition appears and the total emission intensity dramatically decreases. The Raman spectra show clear band at A_{1g}-LA (136 cm⁻¹), E¹_{2g} (248 cm⁻¹), A_{1g} (258 cm⁻¹), in active B²_g (308 cm⁻¹), 2E¹_g (359 cm⁻¹), A_{1g}+LA (371 cm⁻¹), 2A_{1g}-LA (395 cm⁻¹) modes, where LA stands for longitudinal acoustic single degenerated vibrations in the lattice^{5,6}. The PL and Raman spectra of MoSe₂ are shown in Figure S19. The direct A and B excitons of MoSe₂ are at 785 nm and 700 nm respectively. The

peaks at 240 cm^{-1} and 286 cm^{-1} in the Raman spectra of MoSe_2 are the out-of-plane A_{1g} mode and in plane E_{2g}^1 mode respectively.

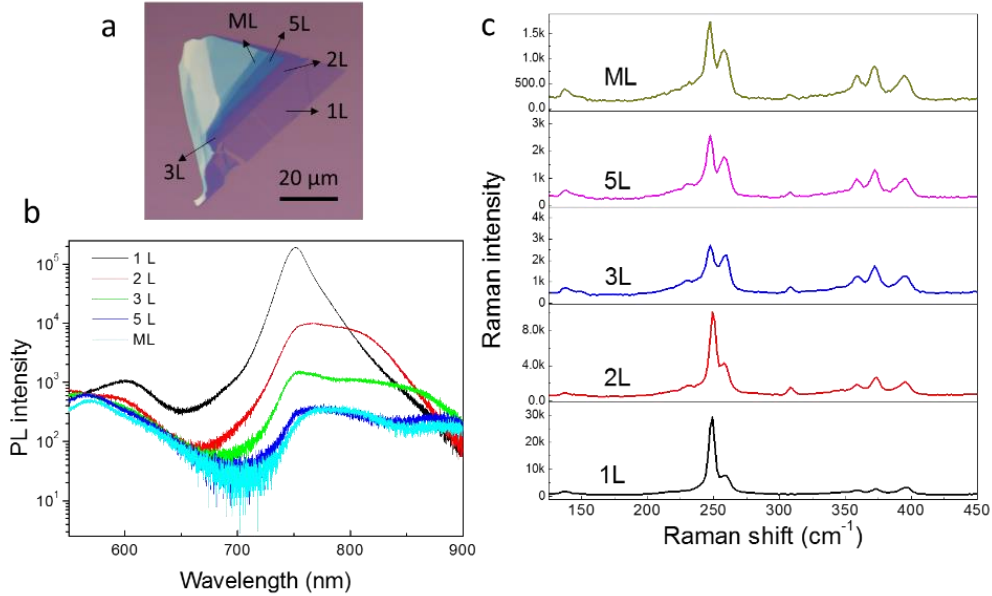


Figure S18: Optical characterization of few-layer WSe_2 . a, Optical image of the WSe_2 flake consisted of different thickness regions. b, PL spectra and c, Raman spectra taken from different regions in the sample.

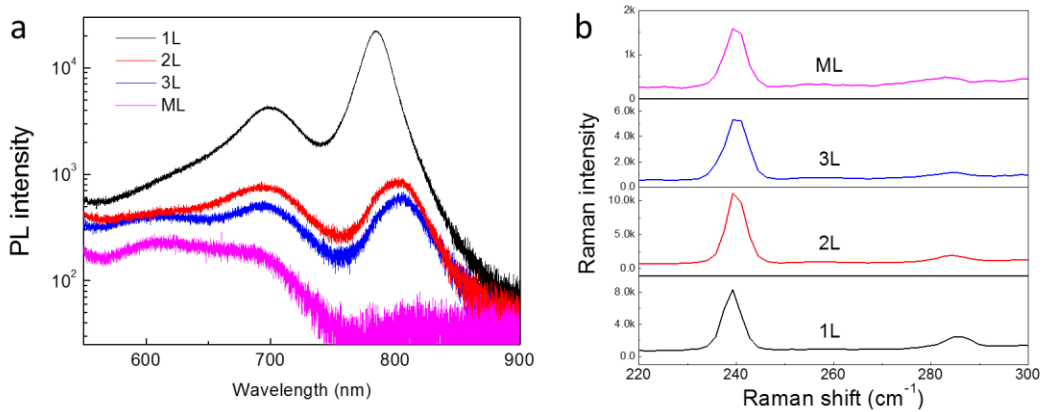


Figure S19: Optical characterization of few-layer MoSe_2 . a, PL spectra and b, Raman spectra of different layers.

12. Raman characterization of controlled area etching

To identify the influence of controlled area etching on sample quality, we used Raman spectroscopy to examine the sample. The optical image of the sample is shown in Figure S20. Few-layer WSe₂ flake was picked up by a top h-BN and transferred to a bottom h-BN. The window of position ‘P3’ was opened through the controlled etching process. The Raman results show no observable change in position ‘P3’ compared with position ‘P1’ and ‘P2’, indicating that the sample was not significantly damaged during the controlled etching process. It’s reported that the doping in TMDCs can influence the position of Raman peak⁷. We did not observe this kind of Raman shift in position ‘P3’, indicating that the sample was not significantly doped during the etching process.

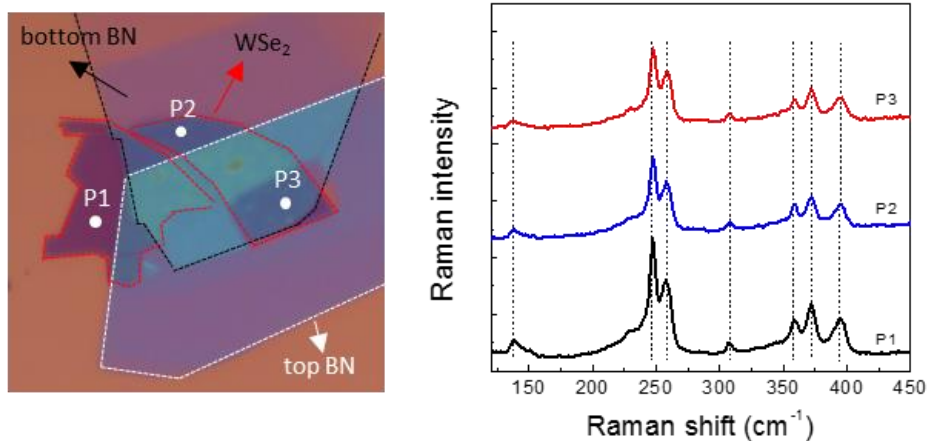


Figure S20: Raman characterizations of few-layer WSe₂ after controlled etching process. a, optical image of h-BN/WSe₂/h-BN sandwiched structure. Position ‘P3’ is opened by controlled etching process. **b,** Raman spectroscopy at different position indicated in (a).

13. Performance summary of h-BN encapsulated TMDC devices

Sample	$\mu_{Field}(T=2K)$ cm ² /V s	$\mu_H(T=2K)$ cm ² /V s	$\mu_{Field}(T=300K)$ cm ² /V s	$\mu_H(T=300K)$ cm ² /V s
WSe ₂ (8L)	8600	7100	104	88
WSe ₂ (5L)	6200	4200	106	57
WSe ₂ (3L)	3900	1334	93	46
WSe ₂ (2L)*	1200		38	
WSe ₂ (p-type)	8550	3300	192	126
MoS ₂ -S1	12700	7900	59	52
MoS ₂ -S2	14000	9900	60	50
MoSe ₂ -S1	4400	1700	40	20
MoSe ₂ -S2	3100	2100	43	34
MoTe ₂ -S1	2300	600	43	31

* Limited by the sample size, four-terminal device was fabricated for 2L WSe₂ sample. Therefore, the Hall mobility for this device was absent.

Table S1: Summary of mobility performance for different samples. For WSe₂ samples, the layer numbers are marked. Other samples are labeled by serial numbers.

14. Angular dependence of the SdH oscillations

The dimensionality of the electronic states can be identified by measuring the angular dependence of the SdH oscillations. Figure S6 shows the magneto-resistance plotted as a function of magnetic fields at different tilt angles θ (between the normal axis of the substrate and B fields). By plotting the derivative dR/dB as a function of $(B\cos\theta)^{-1}$, we find the oscillation depends only on the perpendicular component of the magnetic fields, indicating the 2D nature of carriers in few-layer WSe₂.

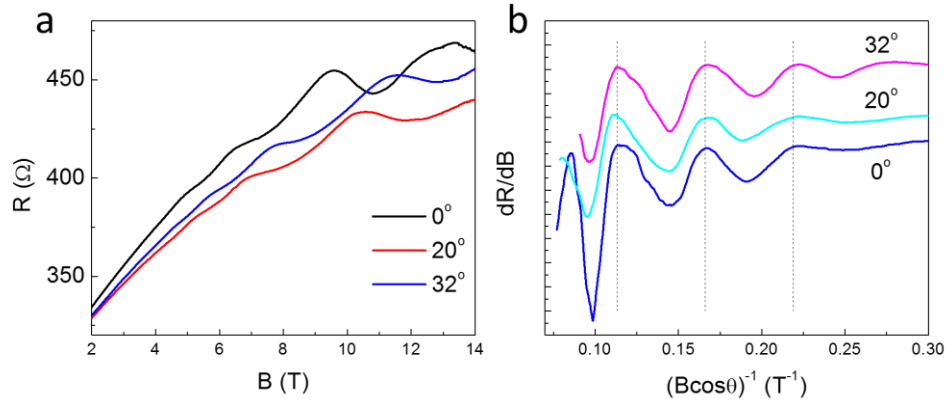


Figure S21: Angular dependence of the quantum oscillations. **a**, Magneto-resistance measured at different orientations with respect to the normal direction of the substrate in a n-type WSe₂ sample. The back gate voltage is kept at 70 V. **b**, Numerical derivative dR/dB as a function of the inverse of the component of B perpendicular to the substrate plane. An offset was added in the curves for clarity.

15. SdH oscillations in few-layer MoSe₂

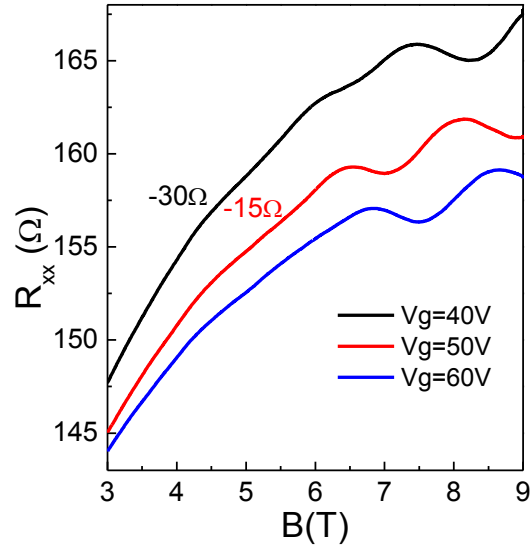


Figure S22: SdH oscillations in a n-type few-layer MoSe₂ sample. Some data were plotted by subtracting a given value for clarity.

References

1. Liu Y, Wu H, Cheng H-C, Yang S, Zhu E, He Q, *et al.* Toward Barrier Free Contact to Molybdenum Disulfide Using Graphene Electrodes. *Nano Lett.* **15**, 3030-3034 (2015).
2. Yu L, Lee Y-H, Ling X, Santos EJG, Shin YC, Lin Y, *et al.* Graphene/MoS₂ Hybrid Technology for Large-Scale Two-Dimensional Electronics. *Nano Lett.* **14**, 3055-3063 (2014).
3. Cui X, Lee G-H, Kim YD, Arefe G, Huang PY, Lee C-H, *et al.* Multi-terminal transport measurements of MoS₂ using a van der Waals heterostructure device platform. *Nat Nano* **10**, 534-540 (2015).
4. Wang L, Meric I, Huang PY, Gao Q, Gao Y, Tran H, *et al.* One-Dimensional Electrical Contact to a Two-Dimensional Material. *Science* **342**, 614-617 (2013).
5. Late DJ, Shirodkar SN, Waghmare UV, Dravid VP, Rao CNR. Thermal Expansion, Anharmonicity and Temperature-Dependent Raman Spectra of Single- and Few-Layer MoSe₂ and WSe₂. *Chemphyschem* **15**, 1592-1598 (2014).
6. Terrones H, Corro ED, Feng S, Poumirol JM, Rhodes D, Smirnov D, *et al.* New First Order Raman-active Modes in Few Layered Transition Metal Dichalcogenides. *Sci. Rep.* **4**, 4215 (2014).
7. Buscema M, Steele G, van der Zant HJ, Castellanos-Gomez A. The effect of the substrate on the Raman and photoluminescence emission of single-layer MoS₂. *Nano Res.* **7**, 561-571 (2014).